Millimeter-Wave Dual Polarized High Isolation Antennas and Arrays on Organic Substrates

Jia-Chi Samuel Chieh, *Member, IEEE,* Binh Pham, *Student Member, IEEE* ,
Anh-Vu Pham, *Senior Member, IEEE,* George Kannell, *Member, IEEE*, Alex Pidwerbetsky, *Member, IEEE*

***Abstract*— We present the design and development of dual polarized aperture coupled stacked patch antennas with substrate embedded air cavities. The antennas, targeted for operation in the W-band (75 – 110 GHz), are realized in a multi-layer organic hybrid substrate utilizing both Kapton and Liquid Crystal Polymer (LCP). Balanced and unbalanced feedlines are investigated in order to improve isolation and mitigate coupling between orthogonal polarized ports. Measured results for the single antenna element show good performance with a beamwidth of 90º and a 2.6:1 VSWR bandwidth of 23 GHz, and isolation of better than 17.8 dB. An 8-element linear array is also designed, fabricated and tested. The antenna array achieves a beamwidth of 13º with a 2.3:1 VSWR bandwidth of 7.2 GHz. Pattern measurements were achieved utilizing a millimeter-wave diode detector circuit implemented directly on the antenna substrate.**

***Index Terms*— Liquid crystal polymer, antenna-in-package, aperture-coupled patch antennas, wide bandwidth, phased-array antennas.**

I. Introduction

THERE has been a major effort in recent years to develop integrated millimeter-wave radio systems. Part of the push has been because of the development of high capacity wireless mobile backhauls which operate in the licensed E-Band (71 – 76 GHz). Recent advances in silicon technology have made possible the realization of multi-antenna phased array radios which are low in cost and small in size [1] – [5]. As there has been advancement in integrated radios, there has also been progress in the development of millimeter-wave antennas. It has been seen that antenna designs for highly integrated millimeter-wave radios have shifted from discrete implementations to chip-scale implementations [6]. This is largely due to the reduced wavelengths at these higher operating frequencies.

Generally two methods are adopted for chip-scale antennas. The first is to build the antennas directly onto a millimeter wave integrated circuit (MMIC) substrate. Slot-ring and microstrip type antennas operating in the W-band (75 – 110 GHz) on a silicon substrate have been reported in [7] – [11]. In these implementations, a quartz superstrate lens or etched horn extensions must be utilized in order to improve the gain. The second method is to implement the antennas on a package level, leveraging organic substrate materials which are more optimal for antenna performance. Zhang *et al.* investigated antenna-on-chip (AoC) and antenna-in-package (AiP) solutions for 60 GHz radios with the conclusion that AoC suffer from low efficiencies due to high permittivity of the silicon substrate rendering AiPs a more desirable solution [12]. Following this work, Liu *et al*. demonstrated several AiP concepts for 60 GHz radios which utilize low permittivity organic substrate materials in order to demonstrate wideband, high gain, and high efficiency antennas [13] – [15]. Two performance metrics which are critical for millimeter-wave antennas are their bandwidth and efficiency. In order to achieve wide bandwidths, substrates with either low dielectric constants or thick dielectric layers must be used [16]. Substrate embedded air cavities have been explored in [17], in order to improve the bandwidth and efficiency. Stacked patch topologies have been investigated in [18] to further improve the bandwidth, even up to the W-Band [19]. The ability to support dual polarizations can also be very desirable. For these applications, high isolation between orthogonal feeds and low cross-polarization is very important. Methods utilizing balun feeds [20] have shown to achieve very high isolation while maintaining low cross-polarization levels.

This paper presents for the first time the development of dual polarized, millimeter-wave aperture coupled stacked patch antennas with substrate embedded air cavities. The use of liquid crystal polymer (LCP) is leveraged because it is light weight [21], near hermetic [22], flexible allowing for conformal designs [23], has a low permittivity and loss tangent stable up to 110 GHz [24], and finally has the ability to support 3D integration [25]. The single antenna achieves a measured beamdwidth of 90º with a 2.6:1 VSWR bandwidth of 23 GHz, covering the 74 – 97 GHz frequency range, the widest bandwidth reported to date. In simulation, the antenna achieves >90% efficiency. This work is also extended to realize an 8-element linear array which achieves a measured beamwidth of 13º and a 2.3:1 VSWR bandwidth of 7.2 GHz, covering the 85 – 92 GHz frequency range.

Section II will discuss the design of the single antenna including the printed circuit board (PCB) stackup, two types of feed-line structures, and finally simulation and measurement results. Section III will discuss the radiation pattern measurement setup and experimental results for the single antenna. Section IV will discuss the design of an 8 element linear array and the associated measurement results. Finally, a summary and conclusion is given in Section V.

Manuscript received Dec. 1, 2012. This work was supported in part by LGS Innovations.

J.S. Chieh is with Spawar Systems Center San Diego, San Diego, CA, 92106 (email: sam.chieh@navy.mil)

B. Pham, and A.V. Pham are with the School of Electrical and Computer Engineering, University of California at Davis, Davis, CA 95616 USA

G. Kannell and A. Pidwerbetsky are with LGS Innovations, Bell Laboratory, Florham Park, NJ, 07932, USA

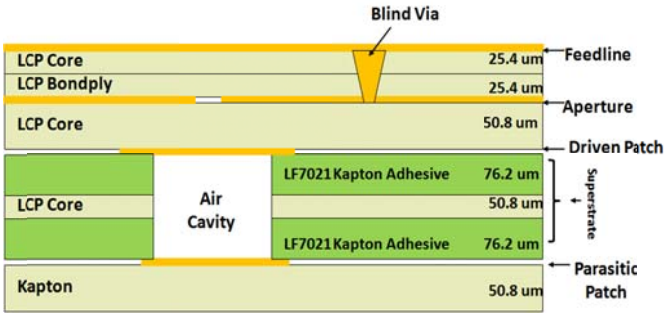

Fig. 1. PCB cross section of proposed aperture fed stacked patch antenna with embedded air cavity.

II. Single Antenna

In the W-band, the frequency is high and the wavelength is small. At 75 GHz the wavelength in free space is 4 mm. In the wafer-scaled packaging scheme, fine lithography and small vias in the order of microns are available. When designing components on a printed circuit board, these fine resolutions are simply not available and pose a serious limitation. Because of this limitation, an antenna feed utilizing a feedthrough via was not an attractive option. Instead, a more elegant and mechanically stable electromagnetic feed was used [25]. Two feed structures are investigated. The first utilizes a general symmetric feedline and achieves nominal isolation between orthogonal polarizations. In the second, a microstrip balun is utilized in order to suppress any orthogonal coupling.

A. PCB Stackup

Fig. 1 shows the PCB stackup for the proposed wideband dual polarized single antennas. The stackup consists of 4 metal layers on a LCP/Kapton hybrid board. Going from the top to the bottom, the antenna feedline resides on a 50.8 µm thick LCP substrate with a dielectric constant $\varepsilon_r \approx 2.94$, loss tangent $\delta \approx 0.002$, and a 17µm double clad rolled copper foil. Directly beneath that is the aperture coupled ground plane. Beneath that is a LCP core layer for which the driven patch metal layer resides. An interleaved Kapton adhesive and LCP layers form the superstrate which give the embedded air cavities mechanical rigidity. Finally, the metallic parasitic patch layer resides on a 50.8 µm thick Kapton substrate with a dielectric constant $\varepsilon_r \approx 3.2$, loss tangent $\delta \approx 0.004$, with a 17µm single clad rolled copper foil. Finally, the blind via illustrated in Fig. 1 is utilized for the grounded coplanar probe launch.

B. Low Isolation Single Antenna Design

Fig. 2(a) shows the first feedline design, for which the horizontal and vertical polarizations are fully symmetrical. The length, width and position of the slot all impact the bandwidth. Generally speaking, when the slot is positioned at the center of the patch, it achieves a much larger bandwidth. However, because dual orthogonal slots are necessary, the slots were positioned near the edges of the patch offset from the center.

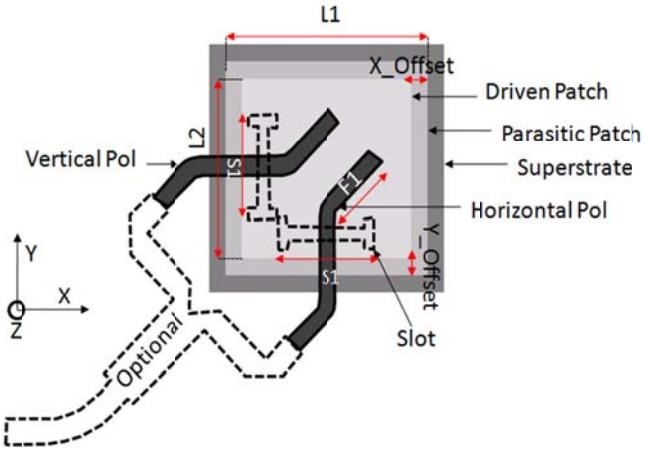

(a)

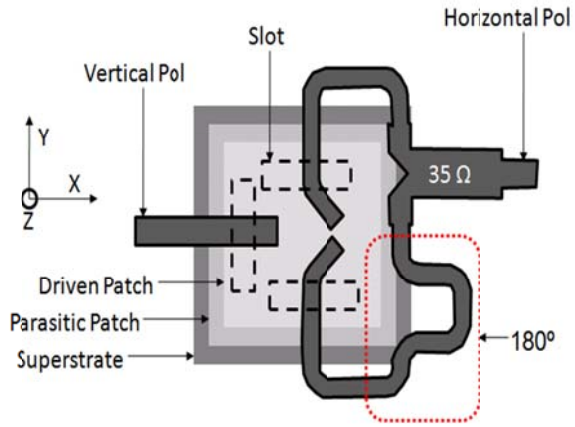

(b)

Fig. 2. Feed structure used in (a) low isolation antenna design (b) high isolation antenna design.

The strategy in improving the bandwidth comes primarily from the use of the stacked patches. Each of the square patches contributes to a resonating frequency. When the two resonances are placed close to each other, they can overlap, extending the overall bandwidth of the antenna. The impedance matching is affected primarily by several parameters including the width and length of the aperture slot, and the length of the open stub feedline. Although the slot length can be tuned, the width is set by the minimum tolerance achievable by manufacturing. In order to gain an understanding of how each of these parameters affects the performance and sensitivity of the antenna, parametric analysis was performed. Fig. 2(a) shows each of the geometries of the antenna that was considered in the parametric sensitivity analysis. The dimensions of the prototype designs are given in Table I and, in each of the following examples, all parameters except for the ones being investigated are held constant to the values given.

The dimensions of the square driven patch and parasitic patch were first considered. Fig. 3 shows simulation results where the driven patch, L1 was varied from 0.71 – 0.8 mm in 30 µm increments and the parasitic patch, L2 was varied from 0.9 – 0.94 mm in 40 µm steps. As can be seen, the bandwidth of

TABLE I
ANTENNA PARAMETERS

Antenna Type	Low Isolation	High Isolation
L1 (μm)	762 x 762	762 x 762
L2 (μm)	950 x 950	950 x 950
S1 (μm)	190	190
F1 (μm)	250	250
Cavity Height (μm)	203	203
Superstrate Size (μm)	1158 x 1158	1158 x 1158

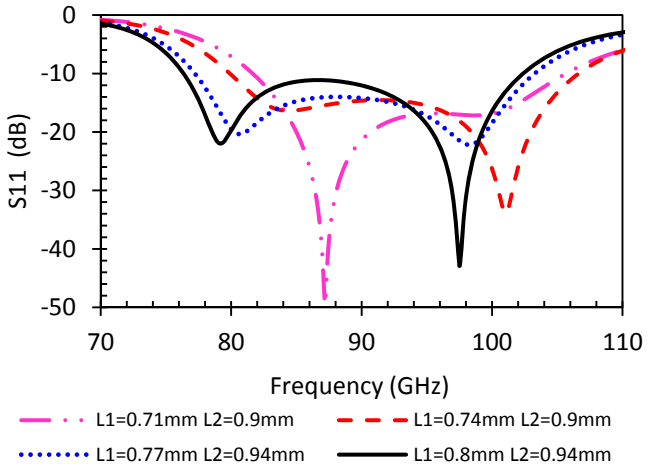

Fig. 3. Simulated reflection coefficient varying the driven and parasitic patch sizes.

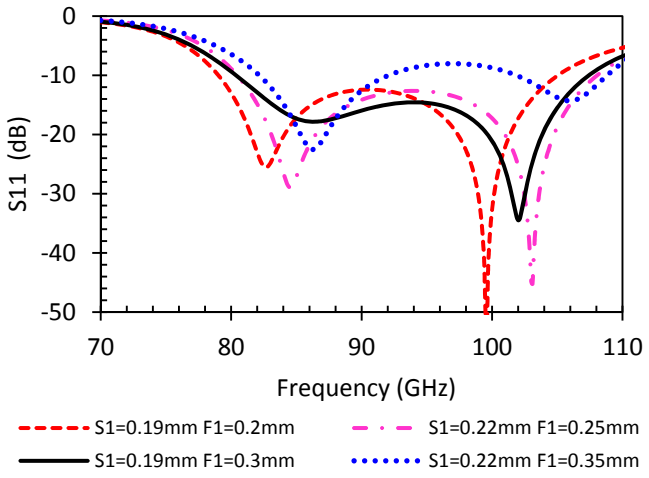

Fig. 4. Simulated reflection coefficient varying the slot length and open stub length.

each of the cases is approximately the same; however the dual resonances is clearly most distinct when the dimensions are exact (L1 = 0.8 mm, L2 = 0.94 mm). 30 μm steps were used as that reflects the absolute minimum tolerance for the PCB process. We also considered the slot length and the length of the open stub feedline. Parametric simulations are shown in Fig. 4. As can be seen, the resonant frequencies can be shifted primarily with the length of the open stub feedline. When the stub length exceeds 0.25 mm, the return loss degrades and

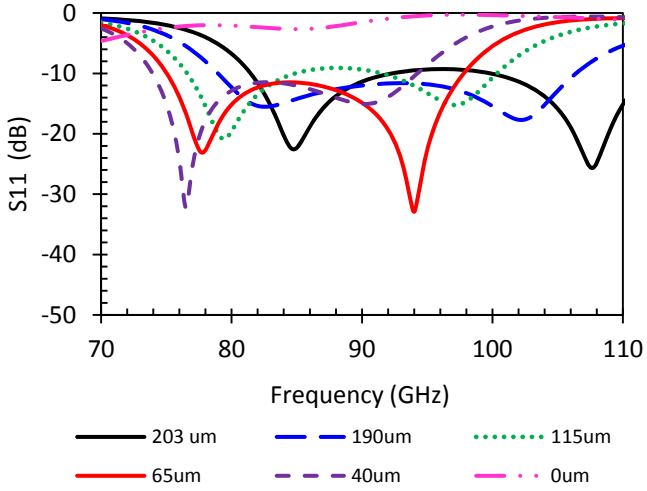

Fig. 5. Simulated reflection coefficient varying the cavity height.

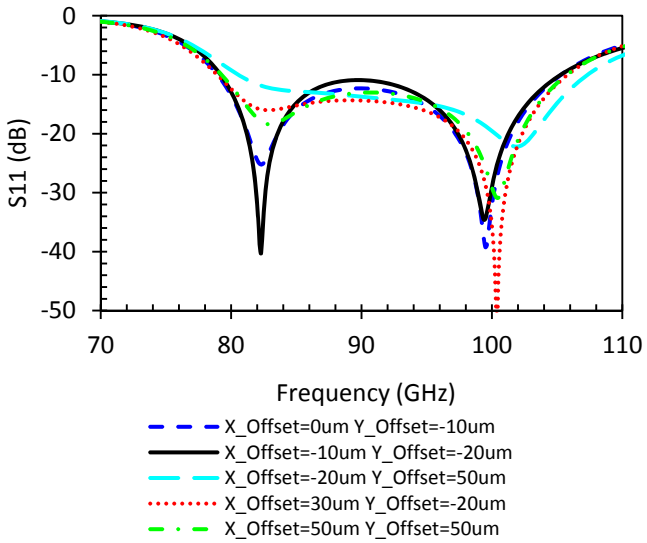

Fig. 6. Simulated reflection coefficient varying patch offset.

bandwidth is reduced. An analysis of the cavity height was also performed; this is shown in Fig. 5. As can be seen, this is one parameter for which the antenna is extremely sensitive to. The optimal height is 203 μm, and as the height is reduced, the 10 dB return loss bandwidth is also reduced. When the cavity is completely filled, the majority of the power is reflected instead of being radiated. Table I shows the optimized parameters for each of the antennas. Using these optimized dimensions we also considered the effects of alignment offsets to the square patches. Fig. 6 shows the simulated reflection coefficients when an offset is added in the *x*-axis and *y*-axis respectively. Even in the most severe circumstance, with a 50 μm offset in both directions, the bandwidth of the return loss remains fairly constant.

In this design, an interleaved Kapton and LCP dielectric material is adopted for the superstrate layer. The reason being that during lamination, LCP has a tendency to flow, therefore

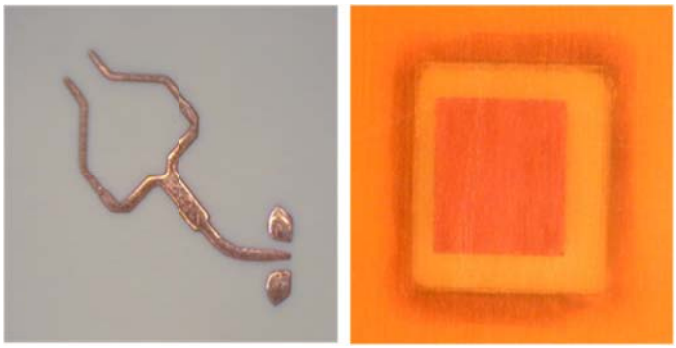

(a) (b)

Fig. 7. Fabricated low isolation antenna design (a) feedline layer (b) top patch layer.

filling the drilled cavities. In order to circumvent this, Kapton adhesive was used to adhere the superstrate layer to the LCP layers. Kapton is a polyimide material that has a much lower lamination temperature and similar dielectric properties, and remains mechanically stable under heat. The height of the air cavity is 203 µm.

The fabricated antenna prototype is shown in Fig. 7. A T-junction power combiner was adopted so that one port measurements could be taken. The ground-signal-ground (GSG) probe pads used for antenna evaluation are grounded coplanar waveguide (CPWG) with a pitch of 150µm. From Fig. 7(b), it can be clearly seen that the top patch is misaligned. In addition, it is noted that the edges of the embedded air cavity are charred from laser ablation.

Since the aperture patch antenna is fed on the opposite side of the radiating patch, probing the antenna for s-parameters is challenging. In order to measure the s-parameters of this antenna on a RF probe station, absorber materials needs to be placed on the chuck to reduce the effects of the metal interface. At the same time, absorber materials are conductive, and so cannot touch the radiating elements either. ECCOSORB HR-10 was used to shield from the chuck and a small cavity was cut so that the antenna would not be in direct contact. The size of the cavity is approximately 30 mm x 30 mm x 15 mm. The test setup is shown in Fig. 8. An Agilent N5251A millimeter-wave network analyzer was used in conjunction with a RF probe station for all measurements.

As can be seen, there are two major dips in the return loss plot. The resonance associated with the first dip is attributed to the parasitic patch, which is larger in size. The resonance associated with the second dip is attributed to the driven patch.

Fig. 9 shows the simulated and measured return loss for the proposed antenna. The simulated 8-dB return loss is about 37 GHz and the measured 8-dB return loss bandwidth is about 19 GHz. The isolation of this design isn't very high because the orthogonal feeds are quite close, and therefore there exists a high level of coupling. Fig. 10 shows the simulated isolation between the two orthogonal ports. As can be seen, it achieves better than 6 dB isolation across the full W-band.

The variation is attributed to the PCB process, which is fairly coarse in resolution. It is also attributed to substrate materials melting and partially filling the cavity during

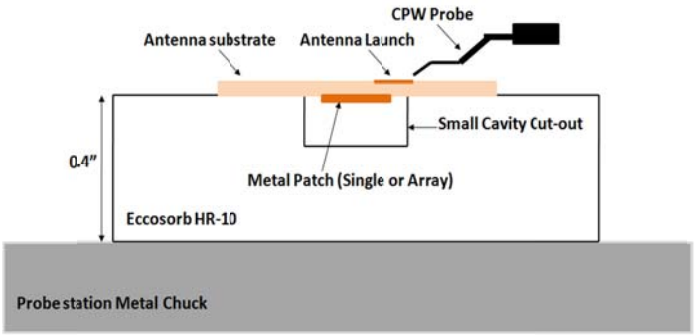

Fig. 8. RF Probe station measurement test setup.

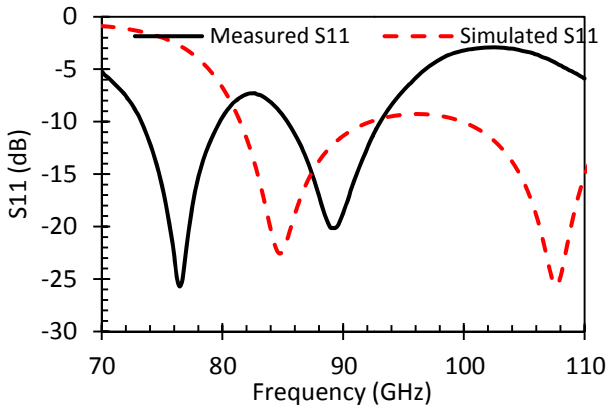

Fig. 9. Simulated and measured return loss of low isolation antenna design.

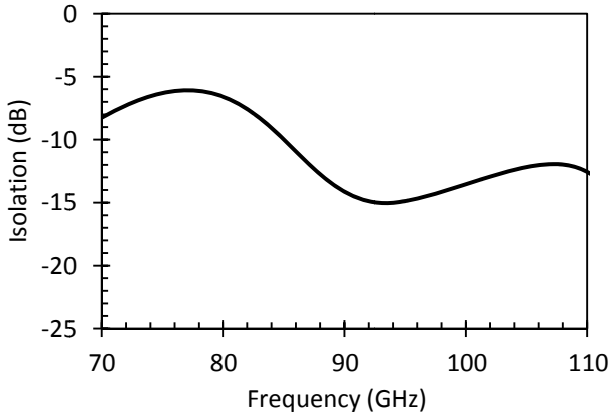

Fig. 10. Simulated isolation between vertical and horizontal ports.

lamination. It is also acknowledged that the absorber foam reduces the effects the metal chuck partially but not entirely

A. High Isolation Single Antenna Design

In order to improve on the isolation and cross polarization levels, an improved design was carried out using a very simple method to achieve feed polarization isolation. This design is shown in Fig. 2(b). The simplest way to increase the isolation between the horizontal and vertical polarizations is to use a differential feed for one of the polarizations. In order to realize this, two coupling slots are used for the horizontal polarization on opposite sides of the patch. Since the coupling slots are on

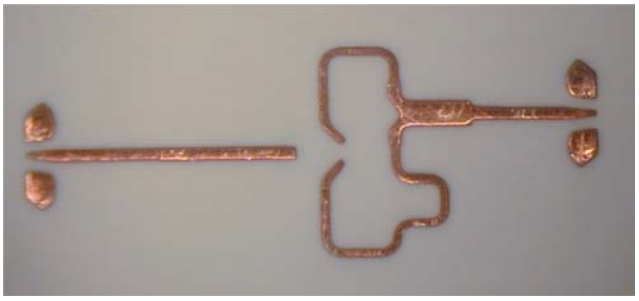

Fig. 11. Fabricated high isolation antenna design showing the feedline layer

opposite sides, they are 180º out of phase with each other. In order to recover the phase for the horizontal orientation, a T-junction combiner is used, for which one side has an additional λ/2 transmission line, effectively acting as a simple balun. Coupling effects from the horizontal to vertical ports, however are in-phase because of symmetry. Therefore with the addition of the 180º phase shift, they are exactly out of phase and therefore are cancelled.

The fabricated antenna shares the same cross-section as in Fig. 1 and the antenna parameters are shown in Table I. The fabricated prototype is shown in Fig. 11. Two port measurements were taken so that isolation between the vertical and horizontal ports could be measured. Fig. 12 shows the simulated and measured return loss for the vertical port. Simulations show a 7-dB impedance bandwidth of approximately 24.8 GHz, while the measurement results show a bandwidth of 24.08 GHz. Fig. 13 shows the simulated and measured return loss for the horizontal port. In simulation the 7-dB bandwidth is about 28 GHz while measurements show a bandwidth of 23 GHz. Measurement results show a slight downward shift in the frequency of operation as well as a reduced bandwidth. Again, this is mainly attributed to the PCB process. It is noted that also in simulation, filling of the air cavity with dielectric also degrades the bandwidth of the antenna. This can occur during the lamination process where the Kapton/LCP walls of the air cavity can melt and fill the cavity. All of these factors can create variation. Fig. 14 shows the simulated and measured isolation between vertical and horizontal ports. As can be seen, the differential feed cancellation operates optimally at the center frequency of the 180º phase shift, this occurs around 100 GHz. In measurement, the isolation between ports is better than 17.8 dB across the entirety of the W-band.

III. Radiation Pattern Measurements

Antenna measurements in the W-Band can be very cumbersome. Researchers tend to adopt three methods. The first utilizes customized probe station setups in conjunction with millimeter-wave extender modules. The second method is by designing a transition from transmission line to a waveguide or coaxial adapter. The third method is to use a high frequency diode detector circuit, which provides a DC voltage output, to measure the radiation patterns. Typical implementations of this method generally utilize self-complimentary or balanced antennas [26], where the diode can

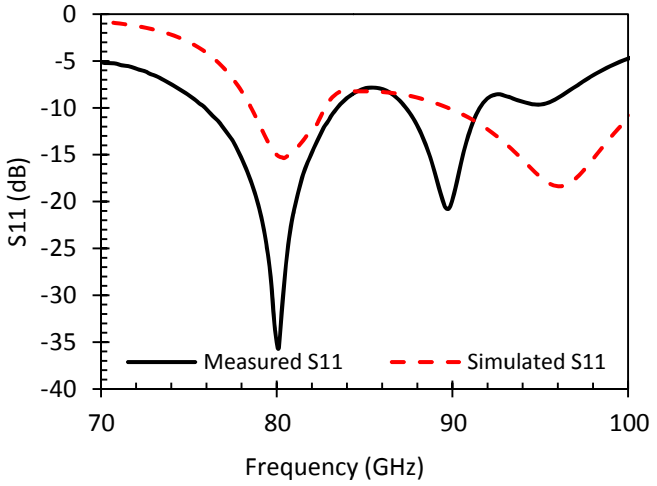

Fig. 12. Measured and simulated return loss for the vertical port.

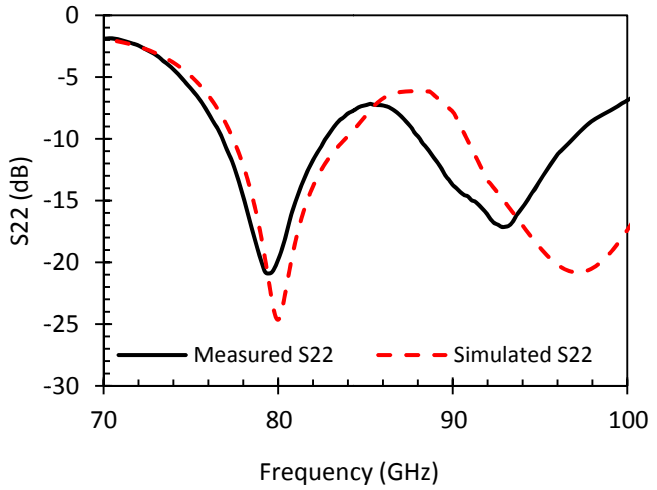

Fig. 13. Measured and simulated return loss for the horizontal port.

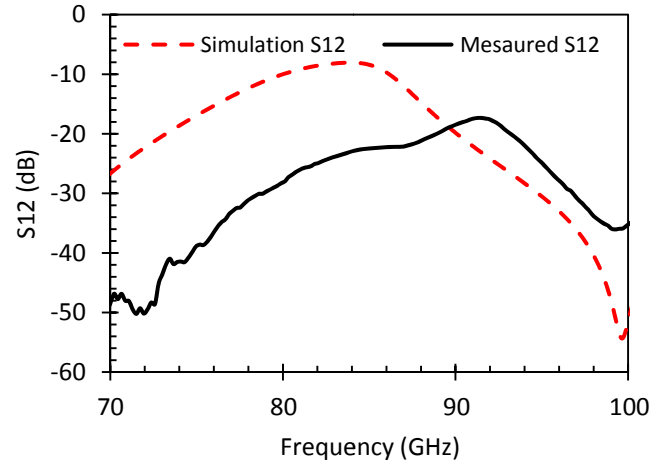

Fig. 14. Measured and simulated isolation between vertical and horizontal ports.

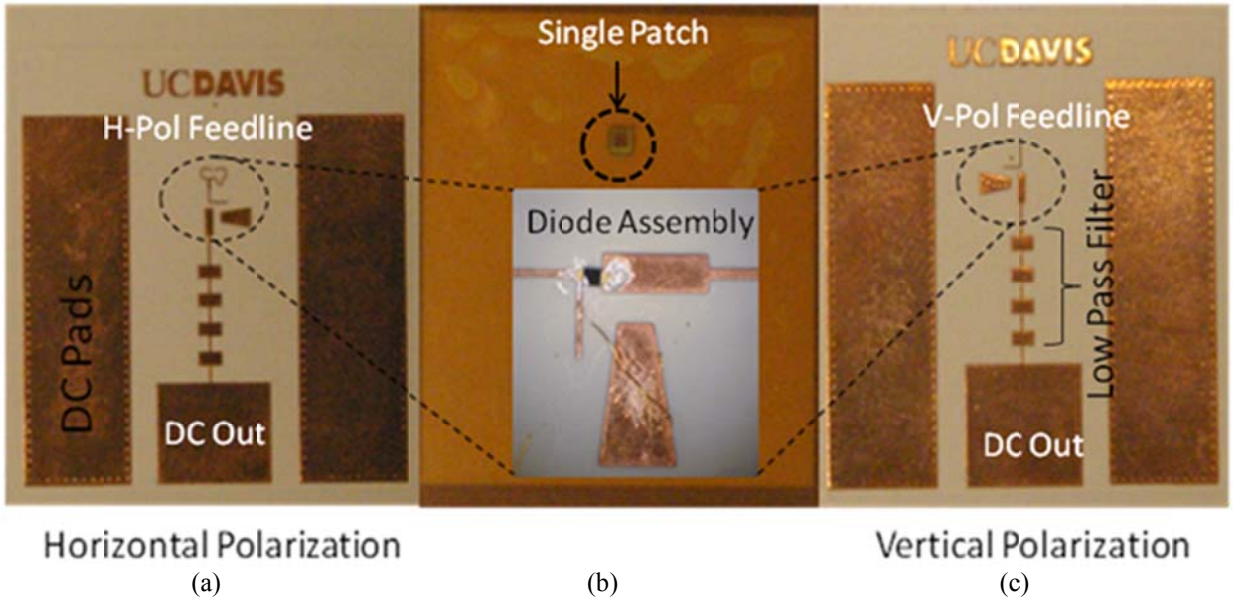

Fig. 15. Test boards for the single antenna element showing (a) horizontal feedline (b) patch antenna (c) vertical feedline

be placed directly in the center without much complication. However, the proposed antennas are singled ended and therefore requires a specialized detector circuit [27].

Fig. 15 shows the test boards for a single antenna element in both the horizontal and vertical polarizations. Immediately following the antenna feedline is a diode detector assembly with a low pass filter (LPF) at the output.

The zero bias Schottky diode used in this work is the MZBD-9161GaAs beam lead diode from Aeroflex, with typical device electrical parameters under forward bias of I_{sat} = 12 μA, R_s = 50 Ω, ideality factor, η = 1.2, and junction capacitance, C_{jo} = 0.03 pF. The beam lead diode is mounted onto the antenna using the combination of an ultrasonic wedge bonder and silver epoxy. In order to provide a DC return, a high impedance λ/2 open stub is placed at the anode, which is bonded from the middle (λ/4) to ground. The bondwire acts as a RF Choke and in this instance a longer bondwire can actually be advantageous.

In order to suppress RF signals from propagating to the output a low pass filter (LPF) is employed. Typical distributed LPFs require a large size to obtain wide stopband rejection. Therefore, a photonic bandgap structure (PBG) was used in order to obtain wide stopband rejection with a minimal size [28].

Fig. 16 shows the experimental setup block diagram for measuring the radiation patterns. A back-wards-oscillator (BWO) is used as a W-band signal source for the transmit horn antenna. A 3 dB WR-10 directional coupler attached to a correct frequency. Because the amplitude of the transmitted signal can be quite low due to limitations of the BWO and losses incurred from free space, a lock-in amplifier is employed in order to improve the sensitivity of the detection system. A 1.8 kHz square wave is used to amplitude modulate the high frequency signal which is necessary for the lock-in system. Although measurement inside an anechoic chamber is

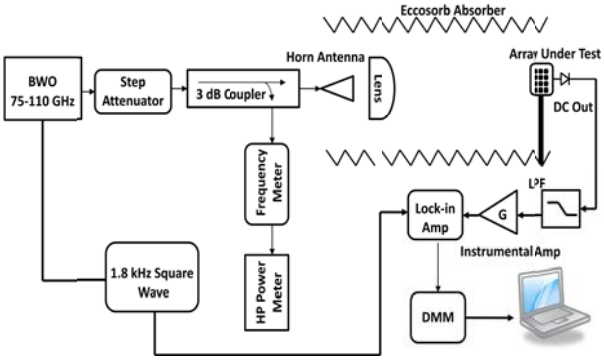

Fig. 16. Block diagram of measurement setup

preferred, this was not possible because the aperture size of the antenna is small, the path length is long, and the transmitted signal is low. For these reasons, a bench-top setup is preferred, where the distance between the transmit antenna and receive antenna can be adjusted. Absorber foam was placed around the test setup to reduce reflections.

Fig. 17(a,b) show the measured *H*-plane radiation patterns for the single antenna element in the horizontal polarization at 95 and 105 GHz. At 95 GHz, the single antenna in the horizontal polarization achieves a beamwidth of 90º, and correlates well with simulation. The measured cross-polarization levels are down by 20 dB from ±90º. Fig. 18(a,b) shows the measured *H*-plane radiation patterns for the single antenna element in the vertical polarization at 95 and 105 GHz. At 95 GHz, the center frequency, the single antenna in the vertical polarization achieves a beamwidth of approximately 90º, which correlates well simulation results. The measured cross-polarization levels are down by 25 dB

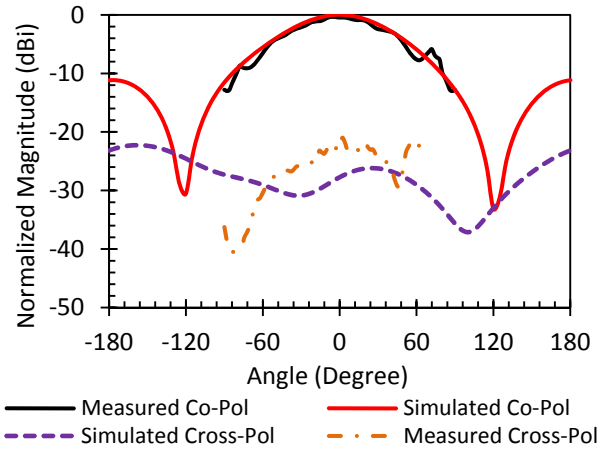

(a)

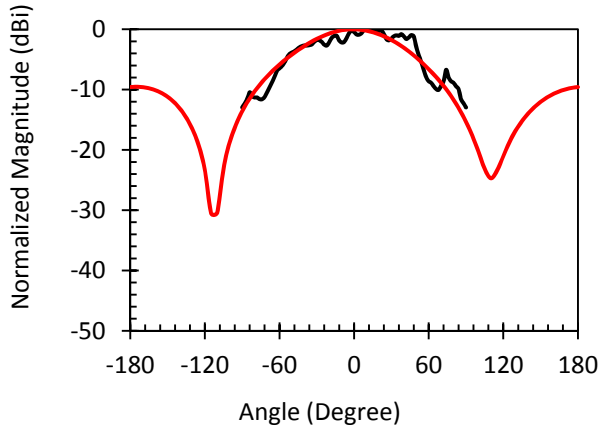

(b)

Fig. 17. Measured and simulated radiation patterns for the horizontal polarization in the *H*-Plane at (a) 95 GHz (b) 105 GHz

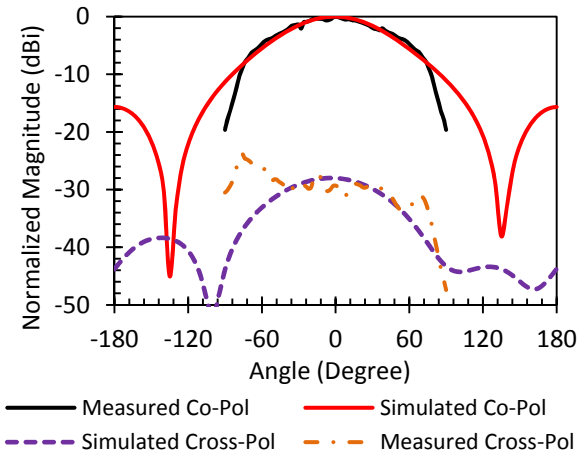

(a)

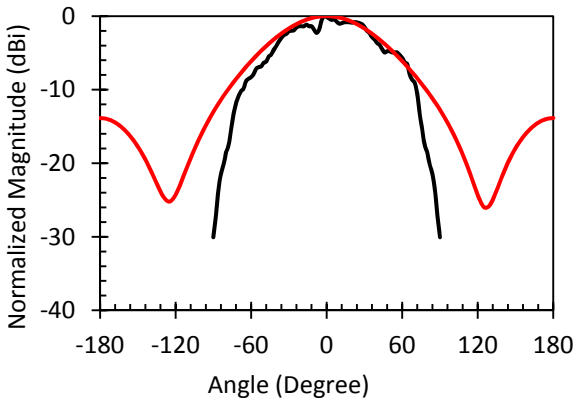

(b)

Fig. 18. Measured and simulated radiation patterns for the vertical polarization in the *H*-Plane at (a) 95 GHz (b) 105 GHz

from ±90º. It is observed that at angles greater than 65º, the radiation pattern has a steep drop-off. This is mainly attributed to scattering effects from various metal surfaces that are present in the table-top setup and low antenna efficiency. The main drawback of this method is that the absolute gain cannot be measured. The simulated gain of the antenna at 95 GHz and 105 GHz are 7.25 dBi and 8.21 dBi respectively. *E*-plane patterns are not presented as the radiating patch is a symmetric structure.

IV. Linear Antenna Array

Based on the high isolation antenna design, an 8-element linear array was fabricated. Utilizing 7 T-junction power combiners, a corporate feed network was design for both the vertical and horizontal polarizations. An antenna inter-elemental spacing of $\lambda_o/2$ was utilized to emulate phased arrayconditions where grating lobes would be minimized. Fig. 19 shows the fabricated antenna array with CPWG launches which are utilized to measure the antenna array. The array was probed in a similar fashion as described in Section II, where absorber foam was placed beneath the array in order to suppress effects of the metal chuck. The loss of a microstrip transmission line is approximately 1 – 1.5 dB/cm across the W-band [24].

Fig. 20 shows the measured s-parameters of the antenna array. It can be seen that the S11 is better than 10 dB from 84 – 92 GHz. The S22 shows a similar behavior being better than 10 dB from 84 – 90 GHz. The deviation is mainly attributed the measurement setup on the RF probe station, which lacks mechanical stability due to the absorber foam. It is also acknowledged that the Kapton adhesive layer thickness, which bonds the air cavity superstrate together, can change after lamination as much as 50% [13], leading to an uneven thickness profile across the array. Finally, the measured isolation between the vertical and horizontal polarization is better than 17 dB across the entirety of the W-band. Fig. 21 shows the measured and simulated *H*-plane radiation patterns in the horizontal polarization at 95 and 105 GHz. Simulated radiation patterns for the array were completed using the finite array synthesis from the single antenna element in HFSS. All pattern measurements of the linear array correlate well with

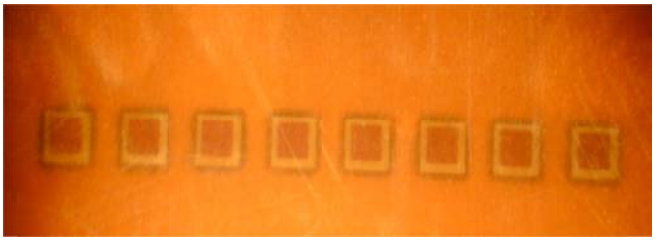

(a)

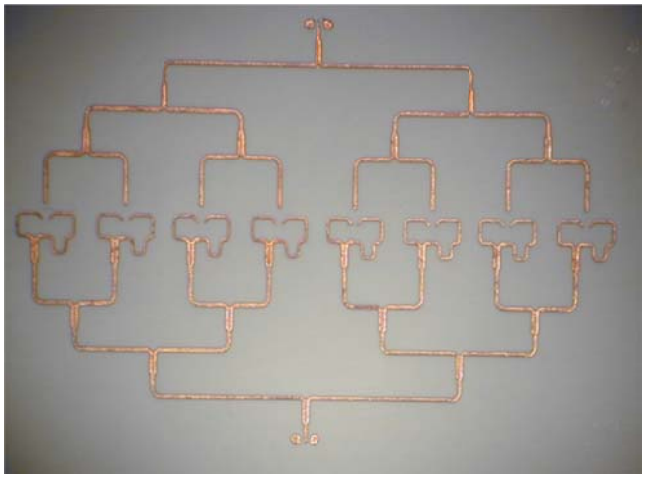

(b)

Fig. 19. Fabricated 8-element dual polarized antenna array (a) radiating patches (b) feedline

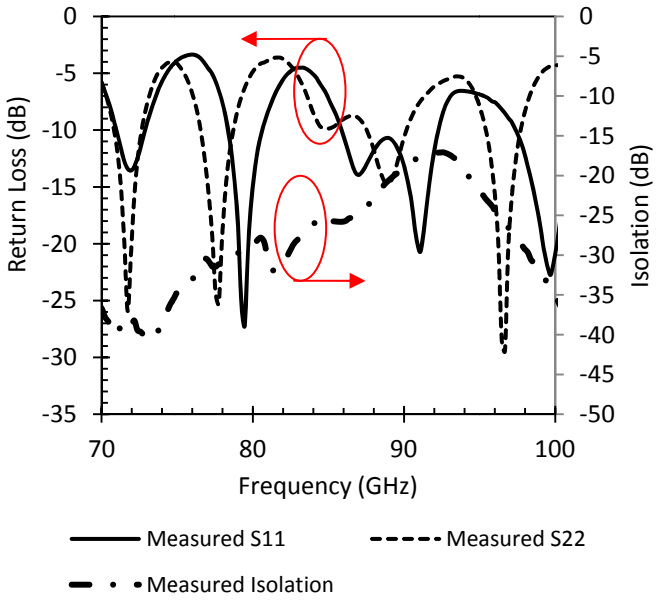

Fig. 20. Measured return loss and isolation of 8-element linear array

simulation results and further validate the operation of the single antenna element. Measured results at 95 GHz show a beamwidth of 13º with a cross-polarization level of less than 20 dB for ±90º. The sidelobes are clearly defined and below the main lobe by more than 13 dB. Fig. 22 shows the measured and simulated *H*-plane radiation patterns in the vertical polarization at 95 and 105 GHz. Measured results at 95 GHz show a beamwidth of 13º with a cross-polarization level of less than 28 dB for ±90º. The sidelobes are also clearly defined and below the main lobe by more than 15 dB. It can be seen that at 105 GHz, the measured patterns are less well formed, especially the sidelobes. However, this is expected as sidelobes degrade faster. This is mainly attributed to poor efficiency of the radiator at the higher frequencies. It is noted that although the efficiency is low at 105 GHz, radiation pattern measurements can still be made primarily because of the dynamic range of the diode detector circuit. It is also noted that the antennas used for probe measurements are not the exact same antennas used for radiation pattern measurements, which utilize a diode detector circuit. For this reason, it is acknowledged that because of variations across the PCB board, antenna characteristic can be slightly different.

Again, because the aperture coupled patch antenna has a feedline and radiating structure on opposite sides, absolute gain measurements are complex and require custom fixtures on the RF probe station that are not available at the time. It is noted that by using pair-wise anti-phase orientations [29], greater cross-polarization suppression can be achieved through the use of symmetry.

V. Conclusion

This paper presents for the first time the development of millimeter-wave dual polarized aperture coupled stacked patch antennas with substrate embedded air cavities which achieve high isolation. LCP is demonstrated as a good candidate material for future millimeter-wave antenna designs. Both a low isolation and high isolation design was demonstrated. The high isolation was accomplished through the use of a balanced feedline. Measured results for this antenna show a 2.6:1 VSWR bandwidth of 23 GHz, covering the 74 – 97 GHz and an isolation of better than -17.8 dB across the full W-Band. In simulation this antenna achieves >90% efficiency.

Extension of this design was also demonstrated with an 8- element linear antenna array. Measured results for this array show an 2.3:1 VSWR bandwidth of 7.2 GHz, covering the 85 – 92 GHz frequency range and an isolation of better than 17 dB. Simulated and measured radiation patterns for the single antenna and 8-element array have also been presented. This antenna is suitable for phased array or fixed beam applications. Furthermore we have demonstrated the feasibility of using standard PCB manufacturing processes for the realization of low-cost millimeter-wave antennas.

Acknowledgment

The authors would like to acknowledge Hai Ta, Cornelius Chin, Huan Liao, Xiangyu Kong, Tianran Liang, and Jiali Lai from the Davis millimeter-wave research center for valuable discussions.

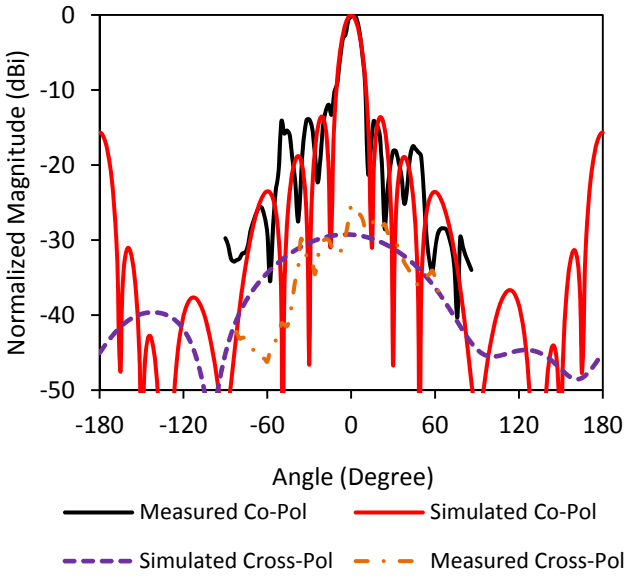

(a)

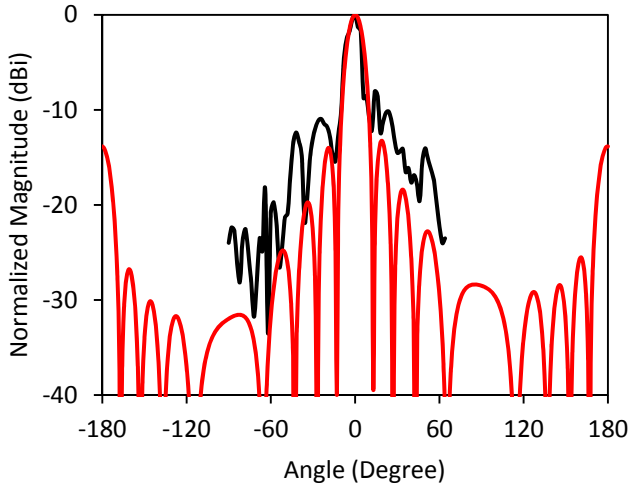

(b)

Fig. 21. Measured and simulated radiation patterns of the antenna array for the horizontal polarization in the *H*-Plane at (a) 95 GHz (b) 105 GHz

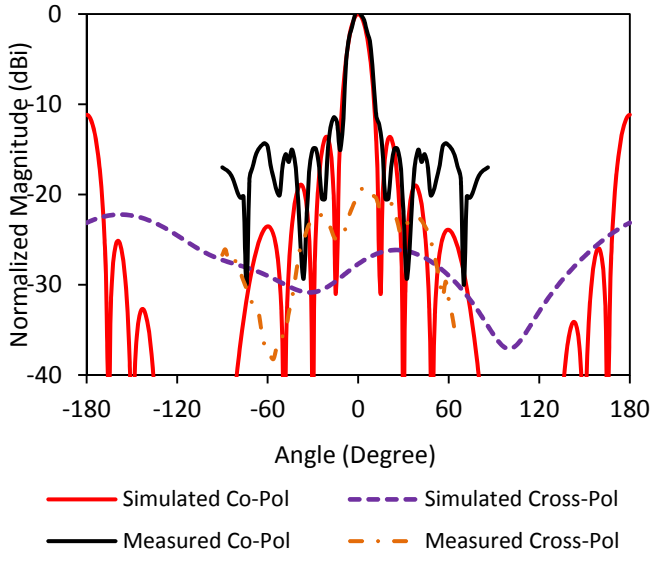

(a)

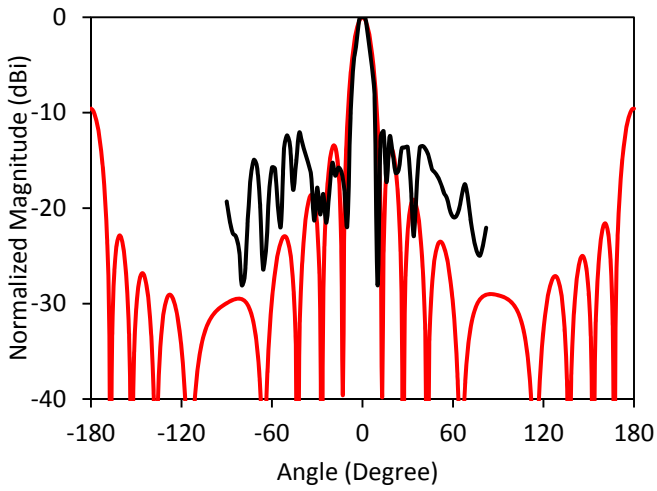

(b)

Fig. 22. Measured and simulated radiation patterns of the antenna array for the vertical polarization in the *H*-Plane at (a) 95 GHz (b) 105 GHz

REFERENCES

[1] Hajimiri, A.; Hashemi, H.; Natarajan, A.; Guan, X.; Komijani, A., "Integrated Phased Array Systems in Silicon," *Proceedings of the IEEE* , vol.93, no.9, pp.1637-1655, Sept. 2005

[2] Kwang-JIn Koh; Rebeiz, G.M., "An X- and Ku-Band 8-Element Phased-Array Receiver in 0.18-um SiGe BiCMOS Technology" *Solid-State Circuits, IEEE Journal of*, vol.43, no.6, pp. 1360-1371, June. 2008

[3] Kwang-Jin Koh; May, J.W.; Rebeiz, G.M., "A Millimeter-Wave (40–45 GHz) 16-Element Phased-Array Transmitter in 0.18-$um SiGe BiCMOS Technology," *Solid-State Circuits, IEEE Journal of* , vol.44, no.5, pp.1498-1509, May 2009

[4] Xiang Guan; Hashemi, H.; Hajimiri, A., "A fully integrated 24-GHz eight-element phased-array receiver in silicon," *Solid-State Circuits, IEEE Journal of* , vol.39, no.12, pp. 2311-2320, Dec. 2004

[5] Natarajan, A.; Reynolds, S.K.; Ming-Da Tsai; Nicolson, S.T.; Zhan, J.-H.C.; Dong Gun Kam; Duixian Liu; Huang, Y.-L.O.; Valdes-Garcia, A.; Floyd, B.A.; , "A Fully-Integrated 16-Element Phased-Array Receiver in SiGe BiCMOS for 60-GHz Communications," *Solid-State Circuits, IEEE Journal of* , vol.46, no.5, pp.1059-1075, May 2011

[6] Pfeiffer, U.R.; Grzyb, J.; Duixian Liu; Gaucher, B.; Beukema, T.; Floyd, B.A.; Reynolds, S.K.; , "A chip-scale packaging technology for 60-GHz wireless chipsets," *Microwave Theory and Techniques, IEEE Transactions on* , vol.54, no.8, pp.3387-3397, Aug. 2006

[7] Raman, S.; Rebeiz, G.M.; , "Single- and dual-polarized millimeter-wave slot-ring antennas," Antennas and Propagation, IEEE Transactions on , vol.44, no.11, pp.1438-1444, Nov 1996

[8] Yu-Chin Ou; Rebeiz, G.M.; , "On-Chip Slot-Ring and High-Gain Horn Antennas for Millimeter-Wave Wafer-Scale Silicon Systems,"

Microwave
Theory and Techniques, IEEE Transactions on , vol.59, no.8, pp.1963-1972, Aug. 2011

[9] Yu-Chin Ou; Rebeiz, G.M.; , "Differential Microstrip and Slot-Ring Antennas for Millimeter-Wave Silicon Systems," Antennas and Propagation, IEEE Transactions on , vol.60, no.6, pp.2611-2619, June 2012

[10] Edwards, J. M.; Rebeiz, G. M.; , "High-Efficiency Elliptical Slot Antennas with Quartz Superstrates for Silicon RFICs," Antennas and Propagation, IEEE Transactions on , vol.PP, no.99, pp.1, 0, *In Press*

[11] Atesal, Y.A.; Cetinoneri, B.; Chang, M.; Alhalabi, R.; Rebeiz, G.M.; , "Millimeter-Wave Wafer-Scale Silicon BiCMOS Power Amplifiers Using Free-Space Power Combining," Microwave Theory and Techniques, IEEE Transactions on , vol.59, no.4, pp.954-965, April 2011

[12] Zhang, Y.P.; Duixian Liu; , "Antenna-on-Chip and Antenna-in-Package Solutions to Highly Integrated Millimeter-Wave Devices for Wireless Communications," *Antennas and Propagation, IEEE Transactions on* , vol.57, no.10, pp.2830-2841, Oct. 2009

[13] Duixian Liu; Akkermans, J.A.G.; Ho-Chung Chen; Floyd, B.; , "Packages With Integrated 60-GHz Aperture-Coupled Patch Antennas," *Antennas and Propagation, IEEE Transactions on* , vol.59, no.10, pp.3607-3616, Oct. 2011

[14] Dong Gun Kam; Duixian Liu; Natarajan, A.; Reynolds, S.K.; Floyd, B.A.; , "Organic Packages With Embedded Phased-Array Antennas for 60-GHz Wireless Chipsets," *Components, Packaging and Manufacturing Technology, IEEE Transactions on* , vol.1, no.11, pp.1806-1814, Nov. 2011

[15] Dong Gun Kam; Duixian Liu; Natarajan, A.; Reynolds, S.; Ho-Chung Chen; Floyd, B.A.; , "LTCC Packages With Embedded Phased-Array Antennas for 60 GHz Communications," *Microwave and Wireless Components Letters, IEEE* , vol.21, no.3, pp.142-144, March 2011

[16] N. Alexópoulos, P. Katehi, and D. Rutledge, "Substrate optimization for integrated circuit antennas," IEEE Trans. Microw. Theory Tech., vol. 83, pp. 550–557, Jul. 1983.

[17] Panther, A.; Petosa, A.; Stubbs, M.G.; Kautio, K.; , "A wideband array of stacked patch antennas using embedded air cavities in LTCC," *Microwave and Wireless Components Letters, IEEE* , vol.15, no.12, pp. 916- 918, Dec. 2005

[18] RongLin Li; DeJean, G.; Moonkyun Maeng; Kyutae Lim; Pinel, S.; Tentzeris, M.M.; Laskar, J.; , "Design of compact stacked-patch antennas in LTCC multilayer packaging modules for wireless applications," *Advanced Packaging, IEEE Transactions on* , vol.27, no.4, pp. 581- 589, Nov. 2004

[19] Lamminen, A.; Saily, J.; , "Wideband stacked patch antenna array on LTCC for W-band," *Antennas and Propagation (EUCAP), Proceedings of the 5th European Conference on* , vol., no., pp.2962-2966, 11-15 April 2011

[20] Shi-Gang Zhou; Tan-Huat Chio; , "Dual linear polarization patch antenna array with high isolation and low cross-polarization," *Antennas and Propagation (APSURSI), 2011 IEEE International Symposium on* , vol., no., pp.588-590, 3-8 July 2011

[21] Chieh, J.-C.S.; Anh-Vu Pham; Dalrymple, T.W.; Kuhl, D.G.; Garber, B.B.; Aihara, K.; , "A light weight 8-element broadband phased array receiver on Liquid Crystal Polymer," *Microwave Symposium Digest (MTT), 2010 IEEE MTT-S International* , vol., no., pp.1024-1027, 23-28 May 2010

[22] Chen, M.J.; Pham, A.-V.H.; Evers, N.A.; Kapusta, C.; Iannotti, J.; Kornrumpf, W.; Maciel, J.J.; Karabudak, N.; , "Design and Development of a Package Using LCP for RF/Microwave MEMS Switches," *Microwave Theory and Techniques, IEEE Transactions on* , vol.54, no.11, pp.4009-4015, Nov. 2006

[23] Symeon Nikolaou; Ponchak, G.E.; Papapolymerou, J.; Tentzeris, M.M.; , "Conformal double exponentially tapered slot antenna (DETSA) on LCP for UWB applications," *Antennas and Propagation, IEEE Transactions on* , vol.54, no.6, pp. 1663- 1669, June 2006

[24] Thompson, D.C.; Tantot, O.; Jallageas, H.; Ponchak, G.E.; Tentzeris, M.M.; Papapolymerou, J.; , "Characterization of liquid crystal polymer (LCP) material and transmission lines on LCP substrates from 30 to 110 GHz," *Microwave Theory and Techniques, IEEE Transactions on* , vol.52, no.4, pp. 1343- 1352, April 2004

[25] Rida, A.; Margomeno, A.; Lee, J.S.; Schmalenberg, P.; Nikolaou, S.; Tentzeris, M.M.; , "Integrated Wideband 2-D and 3-D Transitions for Millimeter-Wave RF Front-Ends," *Antennas and Wireless Propagation Letters, IEEE* , vol.9, no., pp.1080-1083, 2010

[26] Lei Liu; Hesler, J.L.; Haiyong Xu; Lichtenberger, A.W.; Weikle, R.M.; , "A Broadband Quasi-Optical Terahertz Detector Utilizing a Zero Bias Schottky Diode," *Microwave and Wireless Components Letters, IEEE* , vol.20, no.9, pp.504-506, Sept. 2010

[27] Chieh, J.S.; Pham, A.V., Kannell, G.; Pidwerbetsky, A.; " A W-Band 8 x 8 Series Fed Patch Array Detector on Liquid Crystal Polymer", *Antennas and Propagation Society International Symposium (APSURSI), 2012 IEEE*

[28] Taesun Kim; Chulhun Seo; , "A novel photonic bandgap structure for low-pass filter of wide stopband," *Microwave and Guided Wave Letters, IEEE* , vol.10, no.1, pp.13-15, Jan 2000

[29] Shi-Gang Zhou; Tan-Huat Chio; , "Dual linear polarization patch antenna array with high isolation and low cross-polarization," *Antennas and Propagation (APSURSI), 2011 IEEE International Symposium on* , vol., no., pp.588-590, 3-8 July 2011